
Surface currents in the Alderney Race from high-frequency radar measurements and three-dimensional modelling

Lopez G. ^{1,*}, Bennis Anne-Claire ¹, Barbin Y. ², Sentchev A. ³, Benoit L. ¹, Marié Louis ⁴

¹ Morphodynamique Continentale et Côtière (M2C), CNRS UMR 6143, Univ. Caen Normandie, 14000 Caen, France

² Retired from Institut Méditerranéen d'Océanologie (MIO), CNRS UMR 7294, IRD, Univ. Toulon, Univ. Aix-Marseille, 83041, Toulon, France

³ Laboratory of Oceanology and Geosciences, University Littoral Côte d'Opale, Univ. Lille, CNRS UMR 8187 LOG, Wimereux 62930, France

⁴ Laboratoire d'Océanographie Physique et Spatiale (LOPS), CNRS UMR 6523, Univ. Brest, Ifremer, IRD, 29280 Plouzané, France

* Corresponding author : G. Lopez, email address : guiomar.lopez-fernandez@unicaen.fr

Abstract :

Two weeks of high-frequency radar measurements collected at the Alderney Race are compared with the results of a three-dimensional fully coupled wave–current model. Spatial current measurements are rare in this site, otherwise well investigated through modelling. Thus, the radar measurements offer a unique opportunity to examine the spatial reliability of numerical results, and can help to improve our understanding of the complex currents in the area. Comparison of observed and modelled surface current velocities showed a good agreement between the methods, represented by root mean squared errors ranging from 14 to 40 cm s⁻¹ and from 18 to 60 cm s⁻¹ during neap and spring tides, respectively. Maximum errors were found in shallow regions with consistently high current velocities, represented by mean neap and spring magnitudes of 1.25 m s⁻¹ and 2.7 m s⁻¹, respectively. Part of the differences between modelled and observed surface currents in these areas are thought to derive from limitations in the k-epsilon turbulence model used to simulate vertical mixing, when the horizontal turbulent transport is high. In addition, radar radial currents showed increased variance over the same regions, and might also be contributing to the discrepancies found. Correlation analyses yielded magnitudes above 0.95 over the entire study area, with better agreement during spring than during neap tides, probably because of an increase in the phase lag between radar and model velocities during the latter.

Keywords : HF radar, surface current, Alderney Race, MARS 3D, WW3, high-frequency radar

1. Introduction

The Alderney Race is a 15-km-wide strait connecting the Normandy-Brittany Gulf with the central English Channel (figure 1). The circulation in the area is predominantly driven by tides, with weaker contributions from wind and wave forcing, and a negligible effect of density gradients. The tidal regime is a response to the Atlantic semi-diurnal Kelvin wave, which propagates some of its energy into the English Channel [1]. As such, the tidal wave is dominated by the M_2 semi-diurnal constituent [2] and follows a progressive wave regime, with maximum velocities during high and low water. The resonance generated when the Kelvin wave encounters the Contentin Peninsula produces large tidal amplitudes throughout the Normandy-Brittany Gulf. The largest values (approx. 14 m) appear in the Gulf of Mont Saint Michel, and

*Corresponding author

Email address: `guiomar.lopez-fernandez@unicaen.fr` (G. Lopez)

decrease towards the north to amplitudes between 6 and 10 m in the Alderney Race. There, the mean tidal range has been shown to present large horizontal gradients that reach 0.4 m km^{-1} in front of Cap de La Hague [3]. Similarly, water levels show large horizontal variations due to the strong gradients generated by the presence of the Channel Islands, and contribute to accelerating the current [2]. The latter, along with local bathymetric features [4], result in mean spring tide velocities of 2.5 m s^{-1} , and peak velocities in excess of 4 m s^{-1} at the Alderney Race [5]. In addition, the area receives occasional energetic inputs from wind stress and waves [6], which together with an irregular seabed topography varying between 20 and 90 m in short distances [4] induce nonlinear interactions generating a highly turbulent and spatially heterogeneous flow.

Using recent measurements collected with a bottom-mounted current meter deployed at the site, Furgerot et al. [6] observed that the turbulent kinetic energy was 20% larger during ebb tide, despite the higher current velocity measured during the flood tide. They suggested that the turbulence measured during the ebb tide had been generated upstream, and advected southward by the tidal current to their measurement site. In their work, Sentchev et al. [7] and Thiebaut & Sentchev [8] used a towed Acoustic Doppler Current Profiler (ADCP) to obtain one of the few spatial datasets measured at the site. Comparison against the results of a two-dimensional hydrodynamic model evidenced a 20% overestimation in the modelled ebb current speeds over the area where the highest velocities are attained in the strait. This was attributed to the bathymetry resolution and the model's limited ability to reproduce the non-linear effects of tidal wave propagation over highly irregular seabed [8]. Moreover, Sentchev et al. [7] found a high spatial variability on measured current velocity profiles, which shifted from nearly homogeneous to highly sheared over a distance of only 2 km, owing to sharp bathymetric gradients.

Finally, Bennis et al. [9] used a three-dimensional fully coupled hydrodynamic model to simulate the effect of waves on the vertical current profile. They found that, in general, waves tend to reduce the current velocity owing to the effect of Stokes drift in the upper water column and an enhancement of friction at the bottom. Comparing their results with the ADCP measurements of Furgerot et al. [10], they showed their model was able to reproduce the effect of waves on the vertical current profile, which they found to be non-negligible even when the currents were strong (2.3 m s^{-1}). However, they reported a phase delay with respect to measurements that ranged between 0 and 30 min. This was attributed to the effect of bottom friction-generated turbulence and near-bed wave orbital velocity. As evidenced by the studies reviewed in the previous paragraph, these processes can be highly heterogeneous throughout the Alderney Race; hence, it is likely that the results obtained at the ADCP deployment site are not fully representative of the whole area. Thus, observational data able to capture the variability of the site are required to evaluate the model's spatial results and to support further developments in hydrodynamic modelling.

With their ability to generate a spatial snapshot of the surface current with a good compromise between temporal and spatial resolution, land-based high-frequency (HF) radars can provide that kind of data. This remote sensing technology can be particularly useful for monitoring complex coastal settings like the Alderney Race, where the presence of strong currents, an energetic wave climate and a rugged seabed morphology make the deployment of in situ devices a daunting challenge. Measurements acquired with this technology can help to resolve the scales needed to understand the dynamics of tidal circulation and support hydrodynamic modelling, and tidal resource assessments [11, 12].

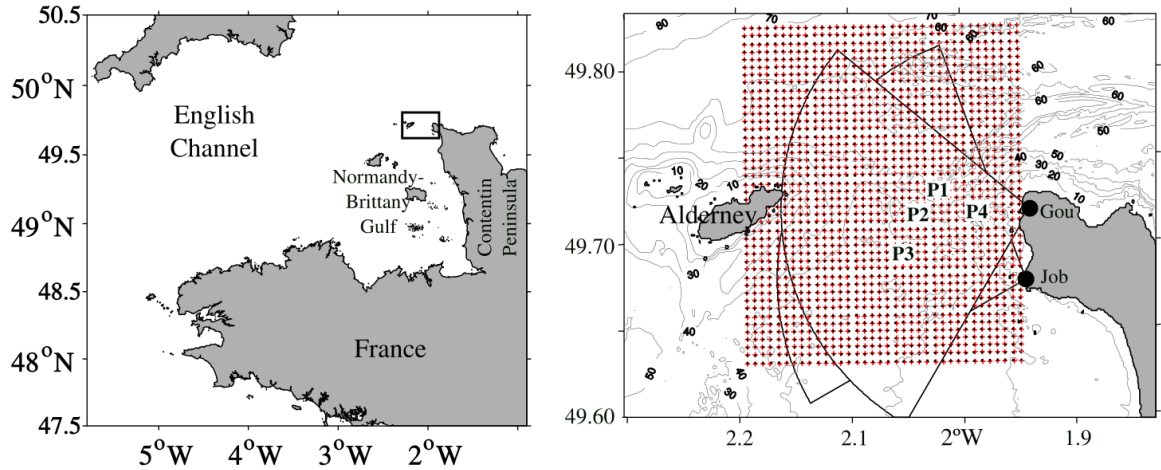


Figure 1: (a) Map of the study area geographical setting and (b) HF radar coverage zone. Depicted in (b) are the radar stations at Goury (Gou) and Jobourg (Job), their maximum coverage for measurements acquired at 24.5 MHz (black arcs) and the measuring grid (black dots). The model grid points used for comparison are shown with red crosses. Points P1-P4 match four grid points with latitude, longitude coordinates, respectively: $(49.7252^\circ, -2.0255^\circ)$, $(49.7117^\circ, -2.0394^\circ)$, $(49.6937^\circ, -2.0533^\circ)$, and $(49.7162^\circ, -1.9907^\circ)$. Bathymetric contours (grey lines) are shown and labelled at 10 m intervals.

Here, we explore the combined use of HF radar measurements and the three-dimensional fully coupled hydrodynamic model of Bennis et al. [9] to draw further insights into their respective results. This work extends the model validation of [9], based on the comparison against ADCP point measurements, by assessing the spatial consistency of the results. Furthermore, we evaluate the current computed at the surface-most layer, where ADCPs are unable to provide reliable measurements because of the effects of side lobes, surface reflection and waves. In addition, we aim to establish the accuracy of the radar surface currents, which, owing to the scantiness of concomitant in situ measurements, have only been evaluated over one tidal cycle, when ADCP measurements were simultaneously available. The results, presented in [13], showed a good agreement between datasets, quantified by a correlation coefficient of 0.96, 21 cm s⁻¹ root mean squared error (RMSE) and a slight positive bias that indicated the radar velocities were on average 6 cm s⁻¹ higher than those of the ADCP.

The article is organised as follows. In the next section we describe the data and methods used to produce the results shown in this document. In section 3 we present the comparison between radar-measured surface current velocities and numerical results. The horizontal structure of the tidal current is then examined in section 4, and the measured and computed residual currents are presented in section 5. Finally, we summarize the results in section 6, and present the conclusions drawn from them in section 7.

2. Materials and methods

2.1. HF radar

A pair of Wellen Radar (WERA) phased-array radars [14] has been installed on the northwest coast of France to characterize the temporal and spatial variability of the Alderney Race. Their measurements constitute the first spatial dataset collected at this site in a continuous fashion, and are aimed at furthering our understanding of the tidal current structure and helping to improve and validate numerical models.

The individual stations are located approximately 5 km apart, at Jobourg and Goury (figure 1). Each site has two four-element transmitting arrays, which operate at 13.5 MHz and 24.5 MHz, respectively, and a 16-element receiving array shared by the two transmitting frequencies. With this arrangement, it is possible to asynchronously operate the radars at the two different frequencies, given the shared receiving array.

The dual transmitting frequency was initially envisaged to allow the full range of sea states that are likely to occur at the site to be measured [15]. Owing to the different wave height thresholds of low and high radio frequencies, the latter is usually only possible using more than one frequency [16]. However, since this work focuses on surface currents, here we use the high resolution measurements acquired at 24.5 MHz. At this frequency, the radar estimation of surface radial currents is based on the spectral analysis of the radio signals scattered off 0.5 Hz ocean waves. These waves (known as Bragg waves) satisfy the condition $\lambda_w = 1/2\lambda_R$, where λ_w is the ocean wave length and λ_R is the radio wave length, and generate two strong peaks (Bragg peaks) in the recorded backscatter spectrum [17], at a relative Doppler frequency determined by their phase velocity and the underlying current [18]. Because the expected Doppler shift due to the phase speed of the Bragg waves is readily derived from the wave dispersion relation, any displacement from this theoretical value is attributed to the surface current.

The dataset used here spans two weeks, from 6 to 22 October 2018. Measurements were collected twice per hour during 8 min 52 s each time, resulting in time series at 30 minute temporal resolution. Range and azimuthal resolutions were approximately 750 m and 7° . In the vertical, the measurements are considered to be a weighted average over an effective depth of 48 cm [19]. The latter is determined as $\lambda_B/4\pi$, where λ_B is the wavelength of the above-mentioned Bragg ocean waves.

The raw measurements were first sorted in range through fast Fourier transform (FFT) [14], and beam forming was then used for azimuthal resolution (further details about the radar data processing are given appendix A). Once the raw signals recorded at each of the two stations were sorted in range and azimuth, radial velocities were calculated over a regular grid at 0.5 km spacing. These were then quality controlled using a de-spiking technique based on the concept of a three-dimensional Poincaré map. The method is based on a graphical representation of the variable and its first and second derivatives. The points located outside of the ellipsoid in the Poincaré map are excluded, and the method iterates until the number of detected spikes becomes zero [20]. This process eliminated 10% of the radial current velocities measured at Goury and 16% of those measured at Jobourg. Then, data gaps were filled using DINEOF (Data INterpolating Empirical Orthogonal Functions) [21]. The latter, is a statistical method that can reconstruct missing data without any a priori information, using the spatial and temporal covariances of the variable under analysis. The method can also be used in a multivariate form, which allows to account for the covariances between variables. Here, we used the latter approach and complemented the radial velocities of the two radars with the water level measured at Dielette in order to enrich the statistics determining the empirical orthogonal functions (EOFs). Before the EOFs were determined, part of the non-missing data were set apart for cross-validation. By comparing this dataset and the reconstructed data, the optimal number of EOFs used for the reconstruction was set to 10. The retained modes explained 90% of the total variance. Correlation between the original and reconstructed velocities was above 0.98 at the four points shown in figure 1, and RMS errors ranged from 0.08 m s^{-1} at P3 to 0.2 m s^{-1} at P2. Finally, the radials of the two stations were combined using a least-squares method [22] to produce surface current vectors throughout the measurement grid (see

appendix A for details).

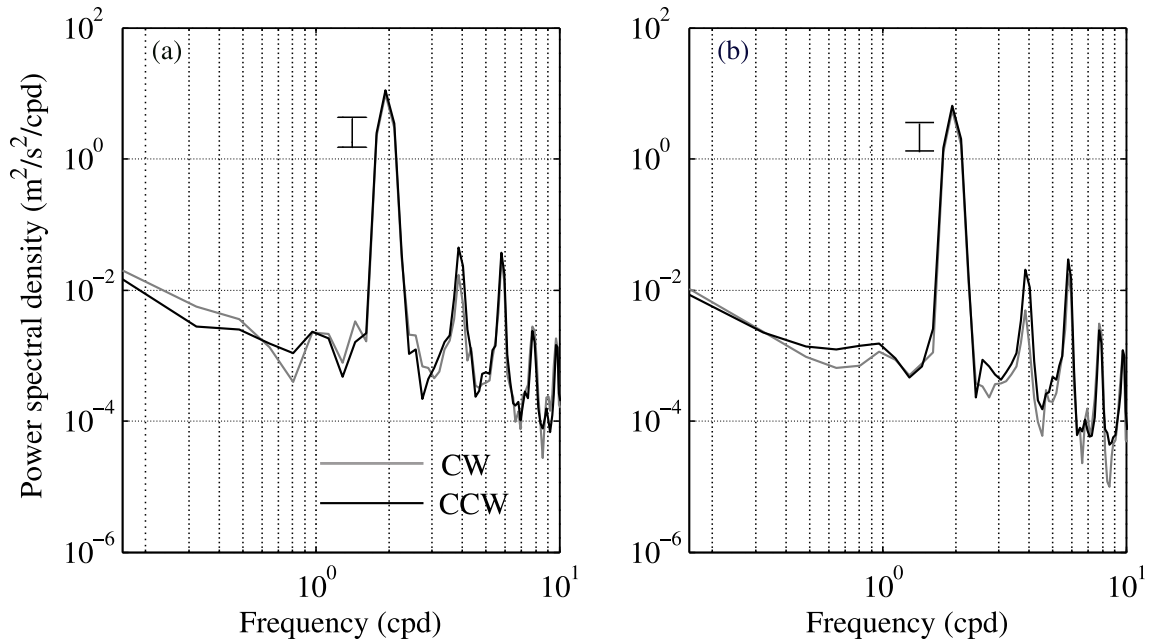


Figure 2: Rotary power spectra calculated from the surface current velocities measured between 6 and 22 October 2018 at (a) P2 and (b) P1. Clockwise (CW) and counter-clockwise (CCW) components are shown in grey and black, respectively. The spectra were estimated using four segments 149 h long with 50% overlap and a Hanning window. The effective degrees of freedom are estimated to be 7. These were calculated as $(8/3)(N/M)$, where M is the length of the time series and N is the length of the window used. The error bar shown in both panels corresponds to the 95% confidence interval.

Figure 2a,b shows the rotary power spectrum of the radar-measured velocities at P1 and P2. The results show the clear dominance of the semi-diurnal tidal constituents, which account for 90% of the variance. Furthermore, the M_2 harmonics (M_4 , M_6 , M_8) dominate the super-inertial band ($f = 1.52$ cpd) above the semi-diurnal frequency, evidencing the importance of non-linearity in the area. The rotary asymmetry is generally low, with predominance of counter-clockwise energy over all frequency bands. The diurnal constituents are weak, and together with the the rest of the sub-inertial band account for less than 0.5% of the variance. Differences in the clockwise components calculated at the two points shown are observed at the low frequencies. These can however be derived from the short period used to calculate the spectra. In addition, the spectral density of semi-diurnal constituents is slightly higher at P2, owing to a bathymetry-induced flow acceleration over a shallow (less than 30 m) rocky plateau located at the centre of the domain.

2.2. Hydrodynamic model

Numerical simulations were performed with a three-dimensional fully coupled wave-current numerical model that combines the three-dimensional hydrodynamic model Model for Applications at Regional Scales (MARS 3D) [23], and the spectral wave model WAVEWATCH-III v4.18 [24]. The flow was simulated for the period 6-22 October 2018, on a grid covering the radar field of view.

MARS 3D solves the hydrostatic primitive equations under the Boussinesq assumption and following the terrain coordinate. WAVEWATCH-III computes the propagation of ocean waves by solving the wave

action conservation equation. Wave forcing is taken into account in the hydrodynamic model with the vortex force method [25, 26] allowing the wave effects on the entire water column to be represented (e.g. Stokes drift effects, enhancement of the bottom friction, changes in vertical mixing). For a wave-forced, three-dimensional, incompressible, unsteady, hydrostatic, constant-density flow, the generic momentum equation is:

$$\frac{D\widehat{\mathbf{u}}_{\mathbf{q}}}{Dt} = \mathbf{S}_{\text{EPGrad}} + \mathbf{S}_{\text{VMix}} + \mathbf{S}_{\text{HMix}} + \mathbf{S}_{\text{WPres}} + \mathbf{S}_{\text{BAcc}} + \mathbf{S}_{\text{BBLay}} + \mathbf{S}_{\text{VForc}}, \quad (1)$$

where $\widehat{\mathbf{u}}_{\mathbf{q}} = (\widehat{U}_q, \widehat{V}_q, \widehat{W}_q)$ is the three-dimensional quasi-Eulerian velocity that is equal to the Lagrangian velocity minus the Stokes drift. The source terms $\mathbf{S}_{\text{EPGrad}}$, \mathbf{S}_{VMix} , \mathbf{S}_{HMix} , \mathbf{S}_{BAcc} , $\mathbf{S}_{\text{BBLay}}$, $\mathbf{S}_{\text{VForc}}$, $\mathbf{S}_{\text{WPres}}$ are for the external pressure gradient, the vertical mixing, the horizontal mixing, the breaking acceleration, the streaming, the vortex force and the wave-induced pressure gradient, respectively. The coupled model has been largely validated for nearshore cases in the past [27, 28, 29], and recently for the Alderney Race [30, 9]. All simulations were two-way with exchanges between both models every coupling time step: MARS 3D sends surface velocities and sea surface height to WAVEWATCH-III, which then sends the wave forcing terms to MARS 3D, and so on. Exchanges were managed by the automatic coupler OASIS [31]. The coupling time steps were different from the model time steps.

Simulations were carried out with the same numerical configuration described in [9], and a bathymetry at 500 m spatial resolution. Two embedded grids with horizontal resolution of 600 and 120 m were used for the parent and the child grids, respectively. The water column was discretized into 15 and 12 vertical levels in the case of parent and child grids, respectively. Both models used the same horizontal resolution. All MARS simulations were three-dimensional, whereas wave simulations were bi-dimensional. MARS 3D was forced at the boundaries by the tidal level of CST France [32]. Sea states were constrained by wave spectra from HOMERE database [33] applied to the boundaries of the WAVEWATCH-III domain. Flow and sea states computed on the child grid have benefited at boundaries from the flow velocity, sea level and wave spectra computed on the parent grid. Wind effects were included via the boundary conditions, but the influence of local wind was not taken into account. This is because the computational domain of the child grid is small enough (47.9011153°N to 50.4583453°N, -0.7272105°W to -6.0596025°W), and the wind intensity was weak during most of the study period, especially over the 3 day time series used here to study spring (811 October) and neap (1720 October) tide conditions. During these 6 days, the wind at 10 m height above the ground recorded at the Goury radar site was below 10 m s⁻¹. Wave effects are included in the surface and bottom boundary conditions. Horizontal mixing is modelled with the Okubo [34] parametrization, whereas the turbulent closure $k - \epsilon$, modified according to [35] to represent wave effects, was used to simulate the vertical mixing.

The time-dependent surface-most level from the modelled water column was selected for the comparisons hereby presented. The latter was extracted from the model grid cells closest to the radars grid cells (figure 1).

2.3. Methods

The agreement between the radar and model-derived velocity fields was investigated using the method of [36], which provides a correlation magnitude equivalent to the determination coefficient, and the angle of

the rotation between the two vectors needed to obtain the highest correlation. In terms of the zonal (u) and meridional (v) current components, the complex correlation is expressed as

$$\rho = \frac{\langle u_1 u_2 + v_1 v_2 \rangle}{\langle u_1^2 + v_1^2 \rangle^{\frac{1}{2}} \langle u_2^2 + v_2^2 \rangle^{\frac{1}{2}}} + i \frac{\langle u_1 v_2 + u_2 v_1 \rangle}{\langle u_1^2 + v_1^2 \rangle^{\frac{1}{2}} \langle u_2^2 + v_2^2 \rangle^{\frac{1}{2}}} \quad (2)$$

where u_1 v_1 and u_2 v_2 are the modelled and radar-measured current components, respectively. The average angle between current vectors is then obtained as

$$\alpha = \tan^{-1} \frac{\langle u_1 v_2 - v_1 u_2 \rangle}{\langle u_1 u_2 + v_1 v_2 \rangle} \quad (3)$$

The calculated angles indicate the counter-clockwise (CCW) rotation of the first dataset from the second. Thus, positive angles mean a CCW rotation of the modelled vector respect to the radar, and vice versa.

In addition, the discrepancies between datasets were also quantified through their RMSE.

$$\text{RMSE} = \sqrt{\frac{1}{n} \sum_{i=1}^n [y_i - x_i]^2} \quad (4)$$

where y corresponds to the modelled value, x is the radar measurement and n is the number of records.

Harmonic analyses of the current were performed with the least-squares method implemented on the `t_tide` Matlab toolbox [37]. Owing to the short length of the dataset, the tidal analysis presented in this document is mainly based on the dominant semi-diurnal tidal component (M_2). However, in order to calculate the current residual, we performed a second tidal reconstruction based on all tidal constituents with signal-to-noise ratios higher than 1. This included 13 constituents, which explained 98.9% of the total measured variance. The coherence between modelled and radar-measured current velocities at the semi-diurnal frequency was calculated following the method described in [38]

$$\gamma_{12}^2(f_k) = \frac{|G_{12}(f_k)|^2}{G_{11}(f_k)G_{22}(f_k)} \quad (5)$$

where G_{11} and G_{22} correspond to the one-sided spectrum of each of the two datasets, $G_{12}(f_k)$ is the one-sided cross-spectrum, and f_k is the frequency of the semidiurnal M_2 tidal component. The results were calculated for two separated periods, covering neap and spring tidal conditions, respectively. In both cases three half-overlapping segments of 24 h were used. The results of the cross-spectral analysis were then used to describe the phase lag between datasets. To characterise the flow kinematics, we calculated the vorticity ($\partial v/\partial x - \partial u/\partial y$) by differentiating the gridded current components using centred differences.

3. Radar - MARS3D velocity comparisons

To examine the concordance between modelled and radar-measured current velocities, the two were compared during a spring and a neap tide, respectively. The statistics of these comparisons are shown in figure 3. During the spring tide (figure 3a-c), complex correlation magnitudes around 0.98 show an almost perfect agreement throughout most of the grid. The lowest values, which are still above 0.97, are found in the centre of the domain, and towards the west. Angular differences are low and negative throughout the radar footprint, indicating a cyclonic rotation of the radar vectors compared to the model. This is inverted in the eastern part of the domain, where there is an average 5° anticyclonic veering of the radar current vectors relative to the model. Finally, the RMSE results show the same pattern of the correlation magnitude (figure

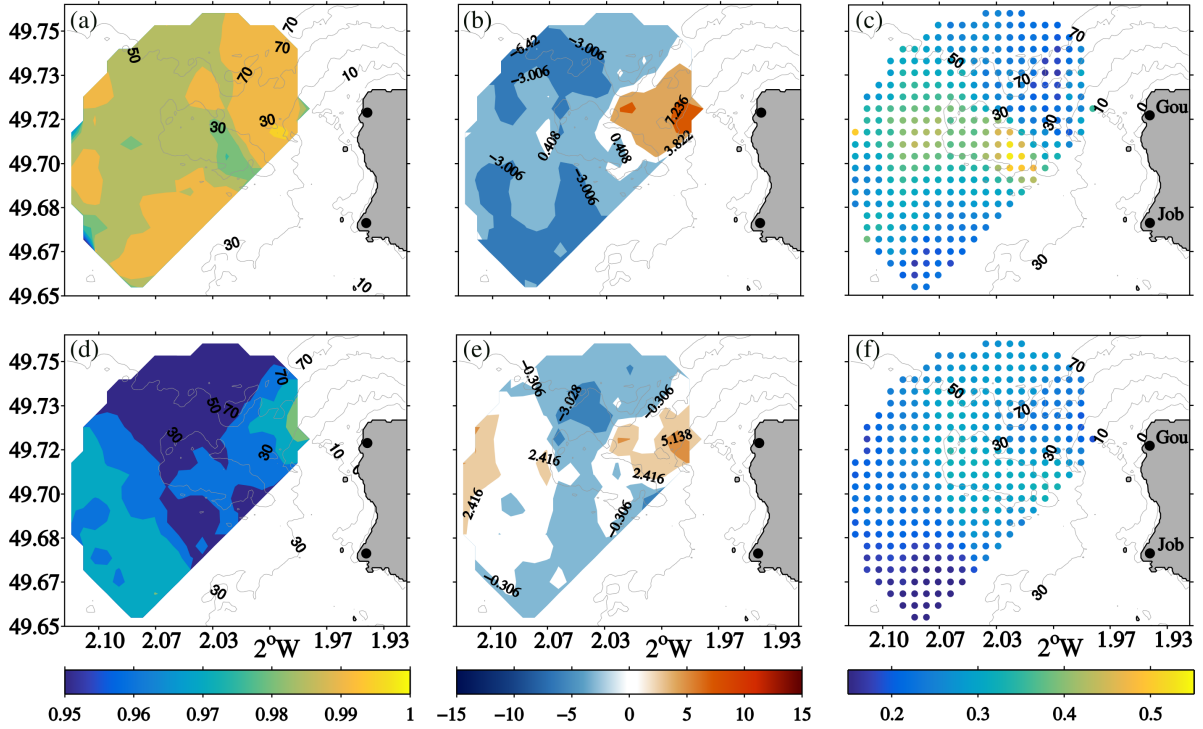


Figure 3: Comparison of model and radar surface current velocity. The first row (a-c) corresponds to spring tide conditions measured between 8 and 11 October 2018. The bottom row (d-f) shows neap tide conditions measured between 17 and 20 October 2018. The first column (a,d) and the second (b,e) are the magnitude and phase of the complex correlation between datasets, and the third column (c,f) is the RMSE. Bathymetric contours (grey lines) and labels (in a, c, d and f) are shown at 10, 30, 50 and 70 m.

3a). That is, the highest errors are found in the areas of lowest correlation, including the area surrounded by the 30-m isobath in the central part of the domain.

During neap tide (figure 3d-f), the correlation magnitude decreased to a minimum value of 0.95 in the northern part of the grid. Otherwise, the distribution of RMSE and veering between modelled and measured current vectors appear to be largely consistent over the fortnightly tidal cycle, and the main difference is a reduction on their magnitudes, which in the case of the RMSE may be due to the weaker current velocities involved in the comparison.

The temporal evolution of the agreement between model and radar current velocity was evaluated at four points within the grid (see figure 1 for their locations). The time series of the spring surface current velocities are shown in figure 4 a-d. There is excellent agreement between datasets at the northern- and southern-most locations (figure 4 a,c) in terms of current velocity magnitude. The phasing between model and radar is low, but there is evidence of a delayed flood reversal in the modelled velocities. At the centre of the domain (P2), the current velocity increases, and so do the differences between radar and model. Notably, the modelled peak ebb velocities attain magnitudes in excess of 0.5 m s^{-1} respect to the radar (figure 4b). Finally, the comparison at the eastern-most point (P4) revealed the highest discrepancies between methods. There, the modelled current velocities exhibit higher asymmetry, with peak flood velocities that exceed the radar measurements in 1 m s^{-1} . This difference reduced to about 0.5 m s^{-1} during the peak of the ebb tide.

The results obtained during the neap tide of 17-20 October 2018 are shown in figure 5. Differences

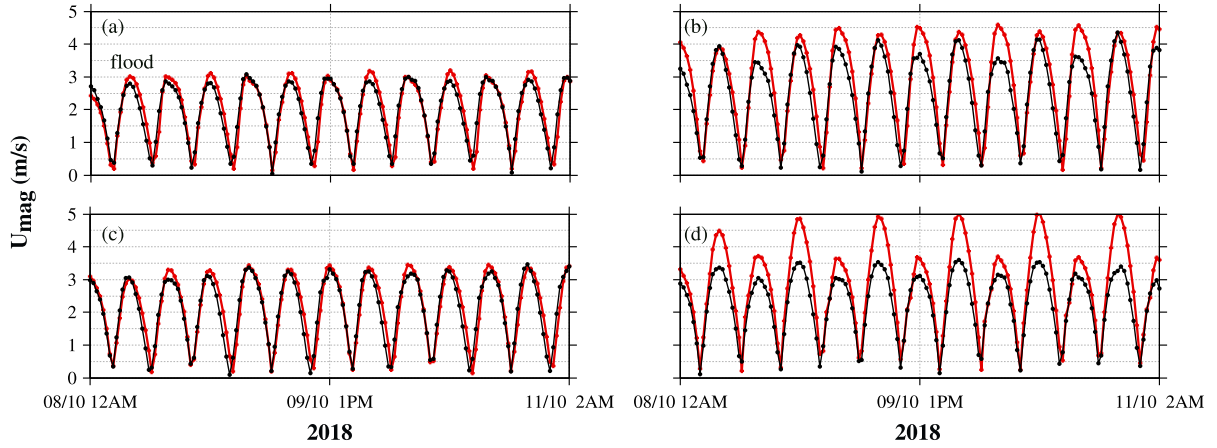


Figure 4: Surface current velocity computed with MARS 3D (red), and measured by the radar (black) during a spring tide over the period 8-11 October 2018. Panels (a-d) correspond to the positions 1-4 shown in 1. The label 'flood' in (a) indicates the peak of the flood tide.

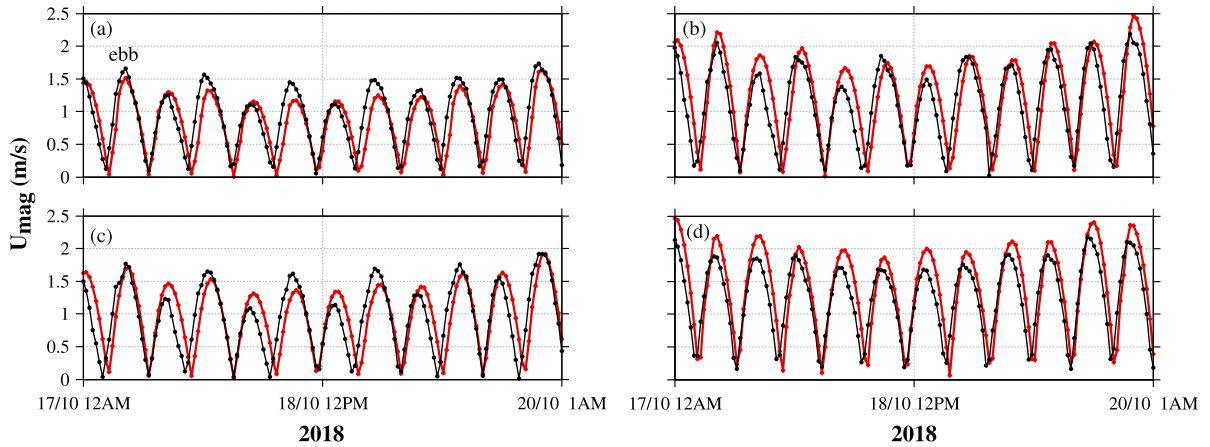


Figure 5: (a-d) Same as in figure 4 but for the measurements collected during the neap tide on 17-20 October 2018. The label 'ebb' in (a) indicates the peak of the ebb tide

between model and radar current magnitudes are variable across the grid. The radar measured slightly higher ebb peak current velocities in the deeper locations at the northern- and southern-most points (figure 5a,c). The differences attain a maximum 0.25 m s^{-1} around the 18 October, when the tidal range was at its minimum (approx. 2 m). The results reverse at the shallower points (P2 and P4), located along the axis of maximum current speeds. There, the modelled peak flood velocity exceeds the radar measurement by a maximum 0.4 m s^{-1} at the point located closest to the headland. Nevertheless, the most evident discrepancy between modelled and measured time series is their phase difference, which probably accounts for the slightly lower correlation values observed in figure 3d during neap tide conditions. Although the value of the delay seems to vary both temporally and spatially, the results indicate that in general, the modelled currents lag the radar measurements. The greatest differences are observed during the flood reversal, which is delayed by 30 minutes respect to the radar results. To examine the spatial distribution of the phase lag, this was calculated at the semi-diurnal frequency as described in the Methods. The results are shown in figure 6. As

already observed in the current velocity time series, the spatial results confirm that higher phase lags occur during the period of lower tidal range (figure 6b) throughout the radar footprint. In addition, the figure shows phase differences that are minimal in front of the headland, and increase offshore to average values of 16° (approx. 30 min) north and south of the 30 m isobath located in the centre of the domain.

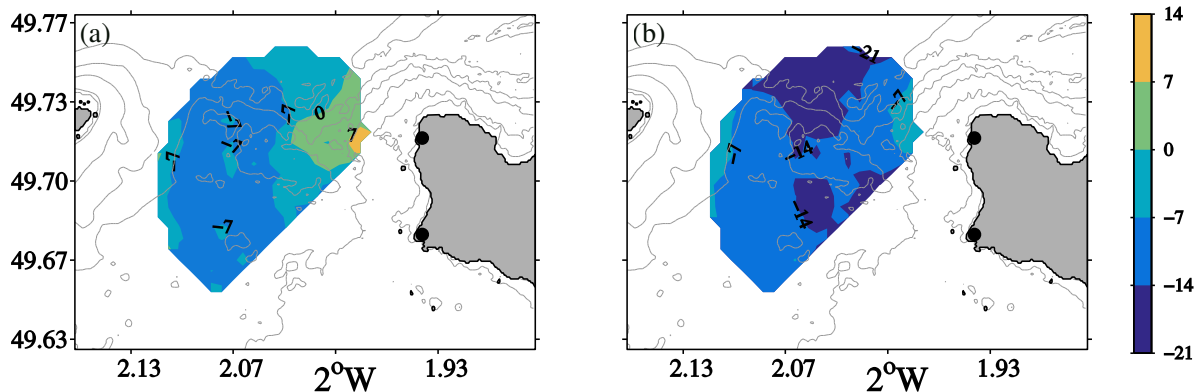


Figure 6: Phase differences (degrees) between modelled and radar-measured currents. Results were calculated for (a) a period covering a spring tide during 8-11 October 2018 and (b) a neap tide from 17 to 20 October 2018.

4. Tidal flow structure

Maps of the measured and modelled M_2 major axis amplitudes and phases are depicted in figure 7. The results evidence good agreement between modelled and measured tidal amplitude patterns (figure 7a-b). Both present higher values in regions where the flow is accelerated owing to bathymetric effects, such as the eastern part of the domain and over the 30 m isobath at its centre. Nonetheless, there is a region within these shallow areas where the model M_2 amplitudes are about 0.5 m s^{-1} higher than the radar's. The ratio of the semi-minor to semi-major axes (not shown) was low throughout the radar coverage, suggesting a close to rectilinear current with semi-minor axes that remain very close to zero but positive, indicating an anticlockwise sense of rotation. The radar's M_2 phase lag with respect to Greenwich varies from 195° in front of the headland to 210° on the western end of the domain, whereas the model phases lag the radar by 10° on average.

The ellipse parameters obtained at the four points depicted in figure 1 are summarized in table 1. There is an excellent agreement between radar and model ellipses at P1 and P3, both in terms of amplitude and inclination. In contrast, the major axis of the modelled ellipse at P4, in front of the headland, exceeds the radar's by 0.6 m s^{-1} . Additionally, whereas the modelled ellipse is mostly rectilinear, the radar M_2 rotation is considerably larger at that point. At P2, the model amplitude is 0.3 m s^{-1} higher, but both ellipses show similar eccentricity.

The spatio-temporal distribution of the surface current was further examined by producing maps at different stages of the tide. These are shown in figure 8, where the surface currents measured on 10 October are depicted at four times, separated by 3 h from each other. During the peak ebb tide (figure 8a,e) the current is directed towards the southwest and the vorticity shows high positive values in front of the headland

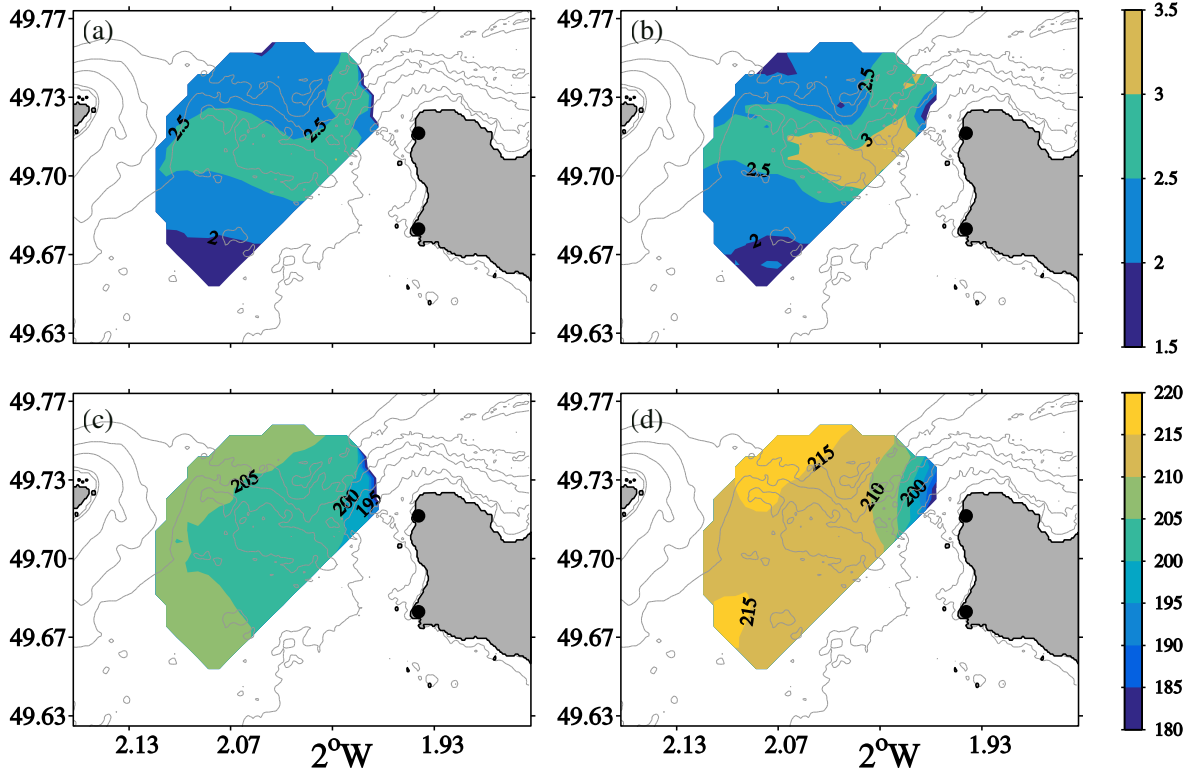


Figure 7: Amplitude (a,b) and phase (c-d) of the M_2 tidal constituent extracted from the the harmonic analysis of (a,c) the radar and (b,d) model datasets.

Table 1: Amplitude (u, v), inclination (θ°), and phase (ϕ°) of the M_2 tidal component derived from the modelled and radar-measured surface currents over the period 6 - 22 October 2018. Results are shown for the points P1-P4 depicted in figure 1. All parameters are shown with the value of the 95 % confidence interval. The last column corresponds to the percentage of the variance explained by the M_2 constituent.

Point	u (m s $^{-1}$)	v (m s $^{-1}$)	θ ($^\circ$)	ϕ ($^\circ$)	$\sigma_{M_2}^2$ (%)
P1					
Model	2.20 ± 0.11	0.10 ± 0.07	60.9 ± 2.16	212.5 ± 2.64	88.6
Radar	2.20 ± 0.06	0.09 ± 0.05	56.31 ± 1.33	203.8 ± 1.6	86.8
P2					
Model	3.19 ± 0.15	0.09 ± 0.1	64.4 ± 2.24	212.8 ± 2.75	89.5
Radar	2.89 ± 0.09	0.09 ± 0.08	63.51 ± 1.5	203.2 ± 1.89	86.0
P3					
Model	2.46 ± 0.14	0.07 ± 0.09	69.2 ± 1.79	213.2 ± 3.11	90
Radar	2.43 ± 0.11	0.08 ± 0.05	71.65 ± 1.07	203.6 ± 2.04	86.2
P4					
Model	3.23 ± 0.19	0.003 ± 0.03	85.9 ± 0.45	206 ± 3.52	88.1
Radar	2.63 ± 0.17	0.09 ± 0.05	76.05 ± 1.26	199.6 ± 3.67	88.1

owing to friction. Three hours later, during the ebb slack (figure 8b,f), the modelled flow is still flowing southward over most of the domain, but shows signs of a developing eddy located in front of Goury. The

radar map is similar, but the eddy that was starting to develop in the modelled flow seems to have been advected westward. During the peak flood tide (figure 8c,g) the current direction is northeast, and the flow is mostly uniform throughout the domain. Interestingly, there is patch of positive vorticity in the radar map which does not appear in the modelled flow. The location of this patch coincides with a very steep gradient in the bathymetry. To reach that point, the current flowing from the southwest has to cross the 30 m isobath to then enter a deep canyon of about 80 m depth, in only few hundreds of meters. The stretching of the water column as the flow crosses the depth contours is probably generating the positive vorticity due to Earth's rotation. The early development of this vorticity appeared 1 h before maximum flood, and it persisted 2.5 h after. The same vorticity patch is not observed in the model results, perhaps because of a smoother representation of the bathymetric step and/or inaccurate modelling of vertical mixing in the area. Finally, during the high tide slack (figure 8d,h) the radar flow has already veered southwest throughout most of the domain, except in the northwest corner. On the other hand, the calculated flow has only begun to turn. An exception to the latter can be observed at a few points close to Goury, where the current is already directed south-westward. This is in accordance to what was shown in figure 6, where the lowest phase lags between model and radar were found in the eastern part of the domain, close to the headland.

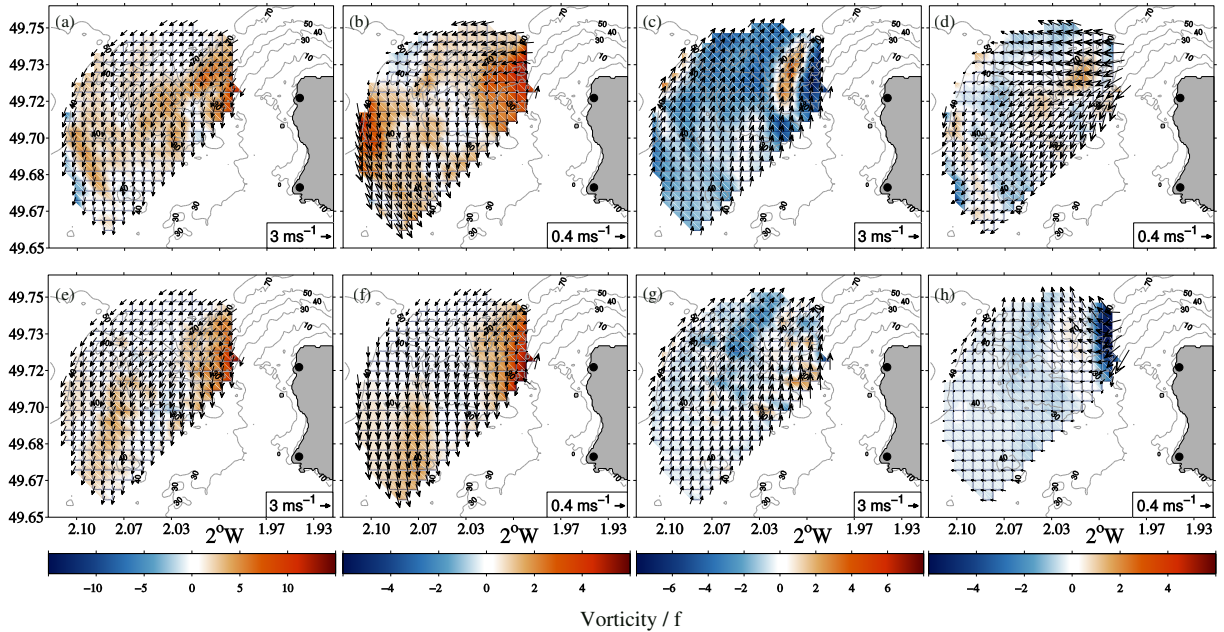


Figure 8: Maps of the surface current vectors overlaid on the relative vorticity field normalized by the Coriolis parameter (f). Results are shown for 10 October, at four stages of the tide: maximum ebb (a,e), low water slack (b,f), maximum flood (c,g) and high water slack (d,h). Results derived from radar measurements (a-d) and the modelled flow (e-h) are shown. The reference arrow shown corresponds to the median current velocity over the domain. Bathymetric contours (grey lines) and labels are shown at 10, 30, 40, 50 and 70 m.

5. Residual flow

The residual components of the surface current depicted in figure 9 evidence a weak residual current, compared with the strong tidal flow. Although the magnitudes of modelled and measured current residual vectors are in close agreement, there is a counter-clockwise rotation of the latter with respect to the former,

at the northern end of the domain. Maximum residual velocities occur in the vicinity of the headland, where there is a north-westward residual flow of about 0.4 m s^{-1} . As observed in the previous section (figure 8), the high topographic gradients in that area induce the production of instantaneous vorticity that is then transferred the residual flow field. Otherwise, measured and modelled residual currents and vorticity show similar patterns, which in turn appear consistent with the circulation associated to the residual eddies generated in the vicinity of the headland, and north and south of the island of Alderney.

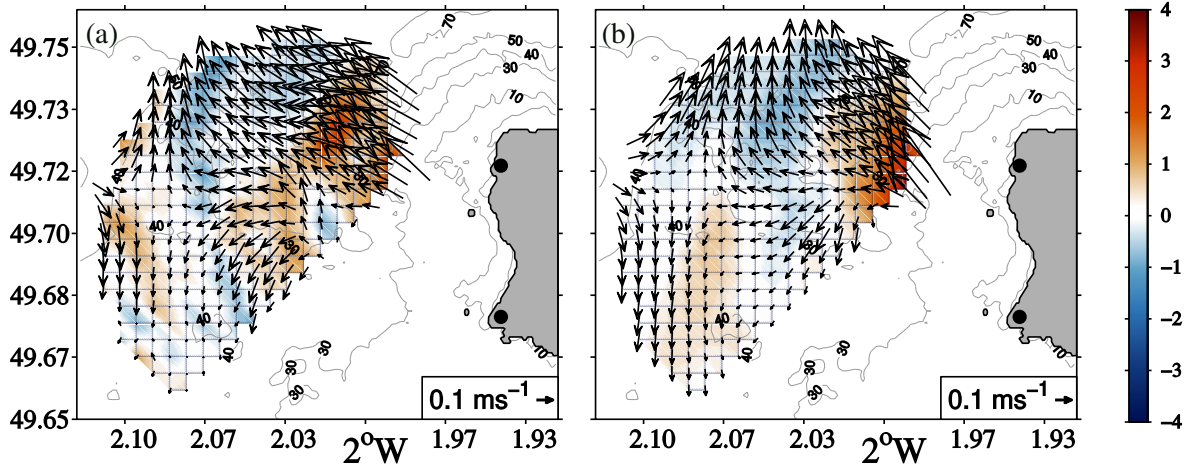


Figure 9: Residual current vectors (m s^{-1}) overlaid on the temporally averaged relative vorticity field normalized by the Coriolis parameter (f). The results are shown for (a) the radar measurements, and (b) the modelled results. The reference arrow shown is the median residual current velocity. Bathymetric contours (grey lines) and labels are shown at 10, 30, 40, 50 and 70 m.

Time series of residual velocities measured at P4 and P2 are shown in figure 10. There is evidence of larger residual flows generated by winds blowing from the north and northeast, which were generally in line with the current and waves during the study period. Under these wind regimes, both the magnitude and modulation of residual velocities increase with respect to south and southwest-blowing winds. Modelled and measured residual velocities show better agreement at P2, whereas the modelled values are generally higher than the observations at P4. There, the modelled zonal component shows sharp peaks of residual velocity approximately 1 h before low water. It seems that modelled nonlinearities generated when the water level is low result in a transfer of energy to the residual flow. On the other hand, the time of meridional peak velocities varies over the two weeks, depending on wind-wave-current directions.

The largest discrepancy between radar and model was observed during the highest wind event registered over the studied period, on the evening of 6 October. At P2 (figure 10d,e), the radar meridional residual current measured before the peak ebb tide, when wind, waves and current were all directed in the same direction (less than 20° apart), was three times larger than the modelled velocity. The effect of the approximately 18 m s^{-1} northerly wind and approximately 2 m waves propagating from the north appears even stronger at P4, where the radar meridional residual current component during flood, when the tidal current opposed wind and waves, was opposite in sign to the modelled result.

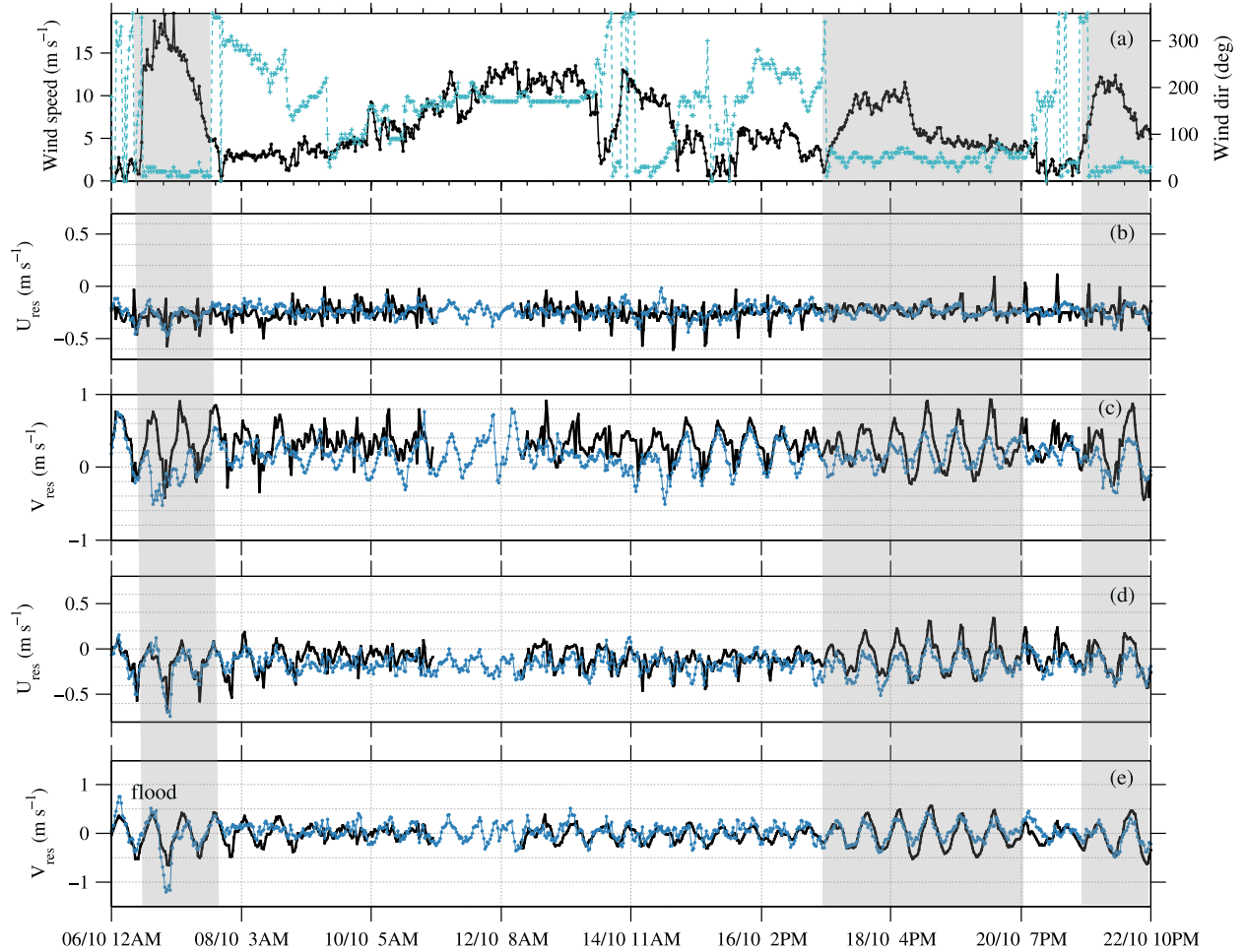


Figure 10: (a) Wind speed (black line and dots) and direction (cyan dashed line and crosses) measured by a LiDAR station located at Goury, and residual current velocity components (m s^{-1}) measured at P4 (b-c), and P2 (d-e). In panels b-e, the blue line with dots is the radar velocity, and the black line is the model. The label 'flood' in (e) indicates the peak of the flood tide. The grey-shaded areas correspond to periods of north and northeast-blowing winds.

6. Summary

The HF radar data collected at the Alderney Race provide a valuable addition to the scarce measurements available at the site, and offer a new opportunity to examine the spatial reliability of numerical simulations. Comparison of the measurements against the results of a three-dimensional fully coupled wave-current model resulted in a good agreement between methods, represented by RMSE ranging from 14 to 40 cm s^{-1} , and from 18 to 60 cm s^{-1} during neap and spring tides, respectively. Maximum errors were found in shallow regions with consistently high current velocities, represented by mean neap and spring values of 1.25 m s^{-1} and 2.7 m s^{-1} , respectively. The hydrodynamic conditions reigning in these areas are challenging for both model and radar. As shown in Appendix A (figure A.11), the radar radial velocities displayed larger variance in areas of steep bathymetric gradients than elsewhere in the radar domain. In these regions, the short ocean waves that scatter the radar-transmitted radio signal are likely to suffer spatial and/or temporal variations during the radar measuring period. This is due to several mechanisms, including shear and fast-varying currents, and will result in the broadening of the radar spectrum [39, 40, 41]. Since the accurate identification of the Bragg peak frequency is central to the determination of radial current velocities, this broadening is associated with

a reduced accuracy. In spite of the latter, the total current vectors were inferred with an average accuracy of 6 cm s^{-1} in these areas (appendix A). Similarly, the model may be limited in its description of the current in areas of high turbulence, owing to an inaccurate representation of turbulence diffusion and related three-dimensional effects during spring tide conditions, when tidal range and current velocity are at their maximum. This might be related to the k-epsilon turbulence model implemented in MARS to simulate vertical mixing, which does not include horizontal advective terms for the turbulent kinetic energy and dissipation (see eqns (2) and (3) of [9]). When the flow velocity is weak (up to 2 m s^{-1}), bottom-induced turbulence is less energetic than for large flow velocities (up to $3\text{-}4 \text{ m s}^{-1}$) and is weakly diffused. In this situation, the turbulent horizontal transport is weak, and the above-mentioned lack of horizontal advective terms for the turbulent kinetic energy and dissipation constitutes a good approximation. However, when the transport becomes strong during spring tides, it can result in strange behaviours. Given that this horizontal transport is induced by the angle between the tidal current and the bathymetry, spurious results might appear during ebb or flood tides, as observed in the results obtained during spring tide conditions at P2 and P4, respectively.

Not surprisingly, the agreement between observed and modelled surface currents improved in areas of smooth topography. Very close to P3, at the point where the ADCP used for validation in [9] was deployed, we obtained NRMSEs (RMSE normalized by the range of measured current velocities) of 0.15 and 0.08 for neap and spring tides, respectively. This compares well with the value of 0.11 found by [9] for a 5 day period of ADCP measurements, characterized by a maximum current velocity of 3 m s^{-1} .

Temporally, the correlation between datasets was better during spring than neap tides. This was due to a phase lag between radar and model velocities. The latter were found to lag the radar, especially during the flood reversal, which was delayed with respect to the measurements. This difference, which was also confirmed when examining snapshots of the current field, has been previously observed when comparing the model results against ADCP measurements, and has been attributed to the underestimation of the effects of wave turbulence in the bottom boundary layer [9]. Bailly et al. [42], who also observed similar phase lags in the results of a two-dimensional hydrodynamic model, stated that the larger discrepancies during neap tides were related to the greater influence of the high-frequency tidal components relative to the semi-diurnal M_2 - S_2 constituents, which during neap tides are out of phase and tend to cancel each other. Our results also point to the latter as the main driver behind the phase differences, which are found to be greater during neap than spring tide conditions, independent of sea state. Nonetheless, within periods of equal tidal range, the lag was also found to vary spatially. In front of the headland, the differences during spring tide conditions were negligible, and increased to about 9 min during the neap tide. The lag increased from this region towards the west, reaching a maximum 30 min during the neap tide. Bennis et al. found [9] that adding local winds in the simulations reduced the discrepancies. The modelled results used here, that included the effect of waves but not that of the local wind, showed the highest phase differences in exposed areas outside the shelter of Alderney. Thus, the spatial pattern of the phase differences can be attributed to the wind and wave bottom stress effects suggested in [9]. In front of the headland, where topographic effects and headland eddy dynamics during tide reversal are important, the relative contribution of wind and waves through bottom stress decrease, and this might result in a corresponding reduction in the delay. However, although we observed increased phase lags during high-wind events (not shown), we did not find a consistent

reduction during calm conditions. Thus, it is not possible to confirm whether the spatial variation in phase lag is due to the model's underestimation of wave-induced bottom turbulence. Furthermore, bearing errors in the radar radial velocities cannot be ruled out.

The semi-diurnal M_2 tide was found to flow through the strait in an almost rectilinear fashion, following its alongshore axis. In shallow areas close to the coast, the modelled M_2 amplitudes exceeded those of the radar, with maximum differences of 0.6 m s^{-1} . Elsewhere, modelled and radar-measured M_2 amplitudes were in good agreement. As opposed to the spatially varying phase differences observed when comparing the measured and computed flows at the semi-diurnal frequency, phase differences in the model and radar harmonic fit of the M_2 constituent were homogeneous throughout the domain, and showed that the model lagged the radar measurements by 10° on average.

The analysis of synoptic maps of the spatial tidal current for different stages of the tide revealed a structure consistent with previous observations of flows near headlands (e.g. [43, 44]), with acceleration of the current in front of the headland, and frictional vorticity generated as the current flows along depth contours with different depths each side. Although vorticity generation in front of the tip of the headland was found to be high during most stages of the tide, the highest values were found during ebb, probably because of a higher effect of bottom friction during times of low water level. Interestingly, during the spring flood tide, the radar current field showed a localized positive vorticity patch in an area characterized by a very steep topographic feature that did not appear in the modelled results. This may be related to either the limitations in turbulence modelling referred to above or an underestimation of the bathymetric step effect in the modelled flow. In this same region, Sentchev et al. [7] found strong gradients on measured current velocity profiles, which shifted from highly sheared over the 30 m plateau located in the centre of our domain to nearly homogeneous at the point where the radar measured a sudden change in the sign of vorticity.

Similar to the tidal current, its residual was found to be representative of analogous geographical settings, characterized by the presence of a headland on one side and an island on the other, and agreed qualitatively well with previous results in the area (e.g. [2, 45]). As such, the two counter-rotating residual eddies generated north and south of Alderney as a result of ebb and flood dynamics were found to meet the residuals associated with the headland at a point located in the western part of the radar domain, where the residual current was found to be negligible. Differences between radar and model residual fields were found in the north part of the domain, and might be associated with radar bearing errors. Close to the headland, the modelled zonal residual component shows evidence of a large amount of energy transferred to the residual flow during ebb. Together with the latter, the tidal origin of the residual flow was evidenced by the modulation of residual velocities over the tidal cycle. Nevertheless, larger residual velocities observed during periods of north and northeastern blowing winds showed an increased influence of wind-driven residual velocities when the angle between current and wind vectors was small. This situation was observed during storm conditions (2 m wave height and 20 m s^{-1} wind speed), which strongly modified the radar residual velocities in front of the headland. At the same location, there were concomitant reductions in peak flood velocities (not shown) that resulted in differences of up to 2 m s^{-1} with respect to the model. Throughout the rest of the domain, wind and waves opposing the current reduced radar peak flood velocities to magnitudes of 0.6 m s^{-1} below the modelled results. Although the modification of current velocity due to waves propagating at low angles from the tidal current has previously been reported (e.g. [46]), the large reduction in current velocity measured

in front of the headland merits further research that is beyond the scope of this paper.

7. Conclusion

We compared HF radar-measured surface currents against the results of a three-dimensional hydrodynamic model with fully coupled wavecurrent interactions. The agreement was found to be very good over most of the domain, and the differences between datasets agreed quantitatively with previous results, obtained by comparing the modelled current against ADCP measurements. Nonetheless, the modelled flood reversal was found to be delayed with respect to the radar. The larger phase lag found during neap tide conditions suggests that its main driver is the higher uncertainty on the source terms during the times of low tidal range.

In spite of overall good results, both datasets used in this study have limitations in regions of large bathymetric gradients and high turbulence. In these areas, the variance of the radial surface currents showed larger values than elsewhere in the radar domain. Similarly, the k-epsilon turbulence scheme implemented in MARS 3D may be limited in its description of the turbulent horizontal transport during periods of strong currents.

Authors' contributions. G.L. performed the data analysis, wrote the manuscript and collaborated on the installation and maintenance of the radar sites. A.C.B. performed the numerical simulations, contributed to the redaction and revision of the manuscript and is the HF radar site director. Y.B. contributed to the project conception, provided expertise and revised the manuscript. A.S. provided expertise and revised the manuscript. L.B. participated in the radar installation and was in charge of their maintenance. L.M. provided expertise, participated in the radar installation and performed their calibration.

Funding. Authors are supported by the HYD2M project (ANR-10-IEED-0006-07) funded by the "Investissements d'avenir" program.

Acknowledgements. The HF radars were bought by Caen University in the framework of the Manche 2021 project, co-funded by the EU and the Normandy County Council, throughout the ERDF-ESF operational programme 20142020. Numerical results were obtained with the Ifremer MARS software, and have benefited from the computing facilities of CRIANN. G.L. would like to thank K.-W. Gurgel for kindly answering questions about his processing software. We also express our gratitude to L. Perez for his assistance on IT related matters. Lastly, we would like to thank the anonymous reviewers who took time to provide comments and suggestions that helped us to improve this manuscript.

Appendix A. HF radar data processing

The radar sites at Goury and Jobourg were synchronously operated in masterslave mode, twice per hour for 8 min 52 s each time. Both transmitted a frequency-modulated continuous wave (FCMW) with 200 kHz bandwidth centred at 24.5 MHz, yielding a range resolution of 750 m. The receiving arrays of both sites were formed by 16 antennas at 6 km spacing (0.495λ), yielding an azimuthal resolution of approximately 7° . However, during this experiment the Goury site was operated with 15 receiving elements due to the malfunction of one antenna. Although this meant an increased sensitivity to side lobes, the defective antenna

was located at the edge of the array; therefore, its exclusion is not expected to significantly affect the quality of the beam forming.

The measurements were processed with the in-house software available with WERA radars as follows. The raw measurements were first sorted in range through FFT. Thereafter, the power spectra of the complex signal were obtained at each antenna. A beam forming technique was then applied for azimuthal resolution, yielding one Doppler spectrum every 1° at each radial ring covering an angular extent of $\pm 50^\circ$ from boresight (direction normal to the receiving array). These spectra were then interpolated onto a Cartesian grid at 0.5 km spacing. For that, the four spectra closest to a grid point were used to obtain the final interpolated result. In the next step, the two strongest peaks (positive and negative) of each Doppler spectrum were identified, in order to infer radial current velocities. The latter were calculated from the power of the spectral lines within an interval of $K = \pm N_{fft}/64$ lines around the two first order peaks (with $N_{fft} = 512$), and their signal-to-noise ratio (S/N) as

$$\overline{u_r} = \frac{\sum_{i=1}^K u_r(i) S/N(i)}{\sum_{i=1}^K S/N(i)} \quad (\text{A.1})$$

where $u_r(i)$ is the Doppler shift of the spectral lines around the first order peak, and $S/N(i)$ is their signal-to-noise ratio. The resolution of these radial velocities is 4.6 cm s^{-1} . This value was obtained as $\delta_{v_r} = \lambda_R \delta_f / 2$, where $\delta_f = 7.5 \cdot 10^{-3} \text{ Hz}$ is the spectral resolution, and $\lambda_R = 12.25 \text{ m}$ is the radio wavelength.

The variance of the radial current velocity, which is related to the width of the first order region, was calculated as

$$\sigma_r^2 = \frac{\sum_{i=1}^K u_r(i)^2 S/N(i)}{\sum_{i=1}^K S/N(i)} - \overline{u_r}^2 \quad (\text{A.2})$$

and, from the above, the accuracy of the radial current velocity was obtained as

$$Acc_r = \frac{\sigma_r}{\sqrt{K}} \quad (\text{A.3})$$

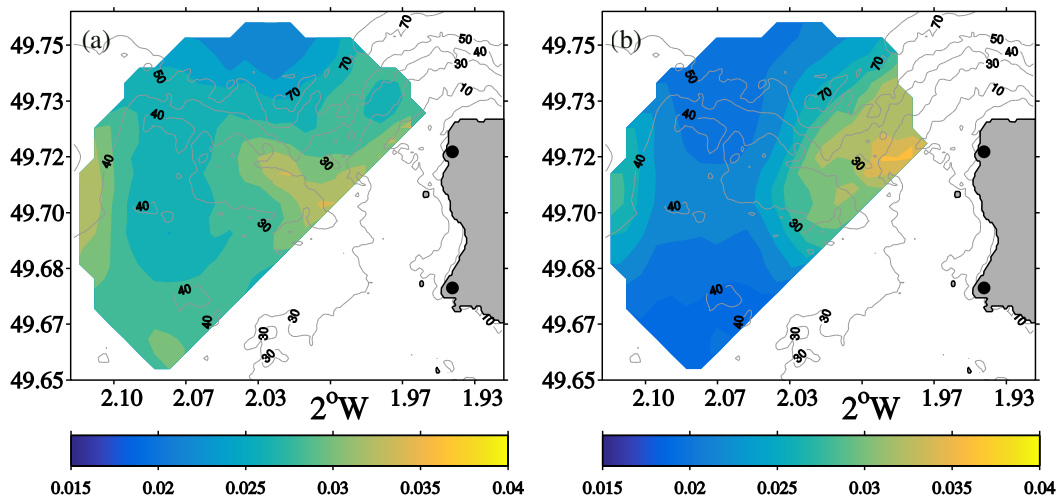


Figure A.11: Time-averaged accuracy (m s^{-1}) of the radial current velocity measured at (a) Goury, and (b) Jobourg during the period 06 - 22 October 2018.

The results of equation A.3 are shown in figure A.11a,b. At Goury (figure A.11a), the radial currents were measured with an average accuracy of approximately 2.5 cm s^{-1} . This value deteriorated to 3.5 m

s^{-1} at a strip following the northern boundary of the 30 m depth plateau, found at the centre of the map. At Jobourg (figure A.11b), the radial current was measured with an average accuracy of approximately 2 cm s^{-1} over most of the domain. Similar to the other site, there is an area of reduced accuracy ($3.5\text{-}3.7 \text{ cm s}^{-1}$), at the eastern-most part of the domain. In both cases, reduced accuracy appears in areas of high bathymetric gradients, where the spatio-temporal variability of the current is expected to be high. This results in the broadening of the Doppler spectral peaks used to infer the radial current velocity, which, as seen in equation A.2, has an effect in the calculation of the radial current variance.

In the last step, the radial current velocities from the two sites were combined to obtain the total current vector. Using the radial current variances calculated with equation A.2, the total surface current was obtained solving equation B5 in [47]

$$(A^T A)u = A^T b \quad (\text{A.4})$$

where

$$A = \begin{pmatrix} \frac{\cos\theta_1}{\sigma_{r1}} & \frac{\sin\theta_1}{\sigma_{r1}} \\ \frac{\cos\theta_2}{\sigma_{r2}} & \frac{\sin\theta_2}{\sigma_{r2}} \end{pmatrix} \quad b = \begin{pmatrix} \frac{u_{r1}}{\sigma_{r1}} \\ \frac{u_{r2}}{\sigma_{r2}} \end{pmatrix} \quad (\text{A.5})$$

Then, the variances of zonal and meridional current components were obtained from the diagonal elements of the covariance matrix C

$$C = (A^T A)^{-1} \quad (\text{A.6})$$

The results of the above expression include the effects of the Geometric Dilution of Precision (GDOP) (figure A.12a), which ranged between 1.5 and 4 over the domain. The surface current accuracy was found to vary from 5 cm s^{-1} close to the coast, to 12 cm s^{-1} at few grid points in the western end of the domain.

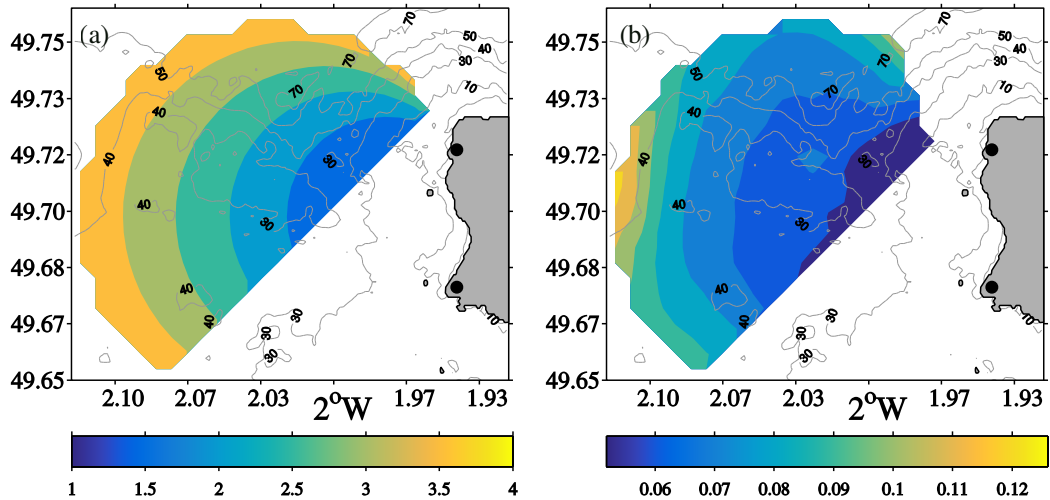


Figure A.12: (a) Geometric dilution of precision. (b) Time-averaged accuracy of the two-dimensional surface currents measured over the period 6-20 October 2018.

References

- [1] D. Pugh, Tides, Surges, and Mean Sea-Level, J. Wiley, Chichester ; New York, 1987.

- [2] A. Orbi, Circulation de maree dans le golfe Normand-breton, Tech. Rep. 84/7480, Ifremer (1986).
- [3] P. Bailly du Bois, M. Morillon, L. Furgerot, C. Voiseux, E. Poizot, Y. Mear, A. C. Bennis, Alderney Race, general hydrodynamic and particular features, *Phil Trans Roy Soc Lond A*(this issue).
- [4] L. Furgerot, Y. Poprawski, M. Violet, E. Poizot, P. Bailly, M. Morillon, Y. Mear, High-resolution bathymetry of the Alderney Race and its geological and sedimentological description (Raz Blanchard, northwest France), *J. Maps* 15 (2) (2019) 708–718. doi:10.1080/17445647.2019.1657510.
- [5] N. Guillou, S. P. Neill, P. E. Robins, Characterising the tidal stream power resource around France using a high-resolution harmonic database, *Renewable Energy* 123 (2018) 706–718. doi:10.1016/j.renene.2017.12.033.
- [6] L. Furgerot, A. Sentchev, P. Bailly du Bois, G. Lopez, M. Morillon, E. Poizot, Y. Mear, A.-C. Bennis, One year of measurements in Alderney Race: What did we learn?, *Phil Trans Roy Soc Lond A*(this issue).
- [7] A. Sentchev, V. T. Nguyen, L. Furgerot, P. Bailly Du Bois, Underway velocity measurements in Alderney Race: Toward a 3D representation of tidal motions, *Phil Trans Roy Soc Lond A*(this issue).
- [8] M. Thiebaut, A. Sentchev, P. B. du Bois, Merging velocity measurements and modeling to improve understanding of tidal stream resource in Alderney Race 178 (2019) 460–470. doi:10.1016/j.energy.2019.04.171.
- [9] A.-C. Bennis, L. Furgerot, P. Bailly du Bois, F. Dumas, T. Odaka, C. Lathuillere, J.-F. Filipot, Numerical modelling of three-dimensional wave-current interactions in extreme hydrodynamic conditions: Application to Alderney Race, *Appl. Ocean Res.* 95, (in press). doi:https://doi.org/10.1016/j.apor.2019.102021.
- [10] L. Furgerot, P. B. Du Bois, Y. Mear, M. Morillon, E. Poizot, A. C. Bennis, Velocity profile variability at a tidal-stream energy site (Alderney Race, France): From short (second) to yearly time scales, in: 2018 OCEANS - MTS/IEEE Kobe Techno-Oceans, OCEANS - Kobe 2018, 2018, pp. 1–8. doi:10.1109/OCEANSKOB.2018.8559326.
- [11] A. Sentchev, M. Thiebaut, Mapping tidal energy resources by High Frequency Radar : Application to resource characterization around the Ushant Island (W . Brittany coast), *Proc. 11th Eur. Wave Tidal Energy Conf.* (2015) 1–10.
- [12] A. Sentchev, M. Yaremchuk, M. Thiebaut, Monitoring Strong Tidal Currents in Straits and Nearshore Regions, in: M. G. Velarde, R. Y. Tarakanov, A. V. Marchenko (Eds.), *The Ocean in Motion: Circulation, Waves, Polar Oceanography*, Springer Oceanography, Springer International Publishing, Cham, 2018, pp. 519–535. doi:10.1007/978-3-319-71934-4_33.
- [13] G. Lopez, A.-C. Bennis, Y. Barbin, L. Benoit, R. Cambra, D. C. Conley, L. Mari, A. Sentchev, L. Wyatt, Surface hydrodynamics of the Alderney Race from HF radar measurements, in: *Proceeding of EWTEC 2019*, Naples, Italy, 1.

- [14] K. Gurgel, G. Antonischki, H. Essen, T. Schlick, Wellen Radar (WERA): A new ground-wave HF radar for ocean remote sensing, *Coast. Eng.* 37 (1999) 219–234.
- [15] C. Maisondieu, Caracterisation statistique des conditions d’etats de mer multimodales dans le golfe de Gascogne pour le dimensionnement des structures en mer., *La Houille Blanche* (6) (2017) 40–48. doi:10.1051/lhb/2017056.
- [16] L. R. Wyatt, J. J. Green, A. Middleditch, HF radar data quality requirements for wave measurement, *Coast. Eng.* 58 (4) (2011) 327–336. doi:10.1016/j.coastaleng.2010.11.005.
- [17] J. Paduan, H. Graber, Introduction to High-Frequency Radar: Reality and Myth 10 (2) (1997) 36–39. doi:10.5670/oceanog.1997.18.
- [18] H. H. Essen, K.-W. Gurgel, T. Schlick, Measurement of ocean wave height and direction by means of HF radar: An empirical approach, *Dtsch. Hydrogr. Z.* 51 (4) (1999) 369–383. doi:10.1007/BF02764161.
- [19] R. H. Stewart, J. W. Joy, HF radio measurements of surface currents, *Deep Sea Res* 21 (1974) 1039–1049.
- [20] N. Mori, T. Suzuki, S. Kakuno, Noise of acoustic Doppler velocimeter data in bubbly flows, *J. Eng. Mech.* 133 (1) (2007) 122–125. doi:10.1061/(ASCE)0733-9399(2007)133:1(122).
- [21] A. Alvera-Azcarate, A. Barth, J. M. Beckers, R. H. Weisberg, Multivariate reconstruction of missing data in sea surface temperature, chlorophyll, and wind satellite fields, *J. Geophys. Res. C Oceans* 112 (C03008). doi:10.1029/2006JC003660.
- [22] E. V. Stanev, F. Ziemer, J. Schulz-Stellenfleth, J. Seemann, J. Staneva, K. W. Gurgel, Blending surface currents from HF radar observations and numerical modeling: Tidal hindcasts and forecasts, *J. Atmospheric Ocean. Technol.* 32 (2) (2015) 256–281. doi:10.1175/JTECH-D-13-00164.1.
- [23] P. Lazure, F. Dumas, An external-internal mode coupling for a 3D hydrodynamical model for applications at regional scale (MARS), *Adv. Water Resour.* 31 (2008) 233–250.
- [24] H. L. Tolman, WAVEWATCH III Development Group, User manual and system documentation of WAVEWATCH III version 4.18, Tech. rep., NOAA/NWS/NCEP/MMAB, College Park, MD, USA (2014).
- [25] F. Ardhuin, N. Rasche, K. A. Belibassakis, Explicit wave-averaged primitive equations using a Generalized Lagrangian Mean, *Ocean Model.* 20 (2008) 35–60. doi:10.1016/j.ocemod.2007.07.001.
- [26] A. C. Bennis, F. Ardhuin, F. Dumas, On the coupling of wave and three-dimensional circulation models: Choice of theoretical framework, practical implementation and adiabatic tests, *Ocean Model.* 40 (3-4) (2011) 260–272. doi:10.1016/j.ocemod.2011.09.003.
- [27] A. C. Bennis, F. Dumas, F. Ardhuin, B. Blanke, Mixing parameterization: Impacts on rip currents and wave set-up, *Ocean Eng.* 84 (2014) 213–227. doi:10.1016/j.oceaneng.2014.04.021.
- [28] A. C. Bennis, F. Dumas, B. Blanke, Modulation of wave-current interactions by horizontal mixing and spatial resolution, *Ocean Model.* 99 (2016) 75–85. doi:10.1016/j.ocemod.2015.12.005.

- [29] S. Moghimi, K. Klingbeil, U. Gr{a}we, H. Burchard, A direct comparison of a depth-dependent Radiation stress formulation and a Vortex force formulation within a three-dimensional coastal ocean model, *Ocean Modelling* 70 (2013) 132–144. doi:10.1016/j.ocemod.2012.10.002.
- [30] A. C. Bennis, P. Bailly Du Bois, F. Dumas, C. Lathuillre, F. Adong, J. F. Filipot, Towards a realistic numerical modelling of wave-current-turbulence interactions in alderney race, in: 2018 OCEANS - MTS/IEEE Kobe Techno-Oceans, OCEANS - Kobe 2018, 2018, pp. 1–7. doi:10.1109/OCEANSKOB.2018.8558790.
- [31] S. Valcke, T. Craig, L. Coquart, OASIS3-MCT User Guide, Tech. rep. (2015).
- [32] R. Leroy, B. Simon, Realisation et validation d’un modele de maree en Manche et dans le golfe de Gascogne - Application a la realisation d’un nouveau programme de reduction de sondages bathymetriques, Tech. rep. (2003).
- [33] E. Boudiere, C. Maisondieu, F. Ardhuin, M. Accensi, L. Pineau-Guillou, J. Lepesqueur, A suitable metocean hindcast database for the design of Marine energy converters, *Int. J. Mar. Energy* 3-4 (2013) 40–52. doi:10.1016/j.ijome.2013.11.010.
- [34] A. Okubo, Oceanic diffusion diagrams, *Deep Sea Research and Oceanographic Abstracts* 18 (8) (1971) 789–802. doi:10.1016/0011-7471(71)90046-5.
- [35] Walstra D. J. R., Roelvink J. A., Groeneweg J., Calculation of Wave-Driven Currents in a 3D Mean Flow Model, *Coast. Eng.* 2000 1050–1063doi:10.1061/40549(276)81.
- [36] P. K. Kundu, Ekman Veering Observed near the Ocean Bottom, *J. Phys. Oceanogr.* 6 (2) (1976) 238–242. doi:10.1175/1520-0485(1976)006<0238:EVONT0>2.0.CO;2.
- [37] R. Pawlowicz, B. Beardsley, S. Lentz, Classical tidal harmonic analysis including error estimates in MATLAB using T_TIDE, *Comput. Geosci.* 28 (2002) 929–937.
- [38] W. J. Emery, R. E. Thomson (Eds.), *Data Analysis Methods in Physical Oceanography*, 2nd Edition, Elsevier Science, Amsterdam, 2001.
- [39] M. L. Heron, Line broadening on HF ocean surface radar backscatter spectra, *IEEE J. Ocean. Eng.* 10 (4). doi:10.1109/JOE.1985.1145128.
- [40] M. L. Heron, E. W. Gill, A. Prytz, An investigation of double-peaked spectra via a convolution/deconvolution algorithm, in: *OCEANS 2008 - MTS/IEEE Kobe Techno-Ocean*, Kobe, 2008, pp. 1–5. doi:10.1109/OCEANSKOB.2008.4530922.
- [41] M. L. Parkinson, Observations of the broadening and coherence of MF/lower HF surface-radar ocean echoes, *IEEE Journal of Oceanic Engineering* 22 (2) (1997) 347–363. doi:10.1109/48.585954.
- [42] P. Bailly, F. Dumas, L. Solier, C. Voiseux, In-situ database toolbox for short-term dispersion model validation in macro-tidal seas , application for 2D-model, *Cont. Shelf Res.* 36 (2012) 63–82. doi:10.1016/j.csr.2012.01.011.

- [43] R. D. Pingree, L. Maddock, Rotary currents and residual circulation around banks and islands, *Deep Sea Res. Part Oceanogr. Res. Pap.* 32 (8) (1985) 929–947. doi:10.1016/0198-0149(85)90037-8.
- [44] R. P. Signell, W. R. Geyer, Transient eddy formation around headlands, *J. Geophys. Res.* 96 (C2) (1991) 2561–2575. doi:10.1029/90JC02029.
- [45] S. P. Neill, J. R. Jordan, S. J. Couch, Impact of tidal energy converter (TEC) arrays on the dynamics of headland sand banks, *Renewable Energy* 37 (1) (2012) 387–397. doi:10.1016/j.renene.2011.07.003.
- [46] M. J. Lewis, S. P. Neill, M. R. Hashemi, M. Reza, Realistic wave conditions and their influence on quantifying the tidal stream energy resource, *Appl. Energy* 136 (2014) 495–508. doi:10.1016/j.apenergy.2014.09.061.
- [47] A. Barth, Ensemble perturbation smoother for optimizing tidal boundary conditions by assimilation of High-Frequency radar surface currents application to the German Bight, *Ocean Sci.* 6 (2010) 161–178.